Understanding the Photocatalytic Reduction of CO 2 with Heterometallic Molybdenum(V) Phosphate Polyoxometalates in Aqueous Media

Youven Benseghir, Albert Solé-Daura, Pierre Mialane, Jérôme Marrot, Lauren Dalecky, Solène Béchu, Mathieu Frégnaux, Maria Gomez-Mingot, Marc Fontecave, Caroline Mellot-Draznieks, et al.

Understanding the Photocatalytic Reduction of CO_2 with Heterometallic Molybdenum(V) Phosphate Polyoxometalates in Aqueous Media.

Youven Benseghir,[⊥,§,‡] Albert Solé-Daura,[§,‡] Pierre Mialane,[⊥] Jérôme Marrot,[⊥] Lauren Dalecky,[⊥] Solène Béchu,[⊥] Mathieu Frégnaux,[⊥] Maria Gomez-Mingot,[§] Marc Fontecave,[§] Caroline Mellot-Draznieks,*[§] and Anne Dolbecq*[⊥]

[⊥] Université Paris-Saclay, UVSQ, CNRS, Institut Lavoisier de Versailles, 78000, Versailles, France.

[§] Laboratoire de Chimie des Processus Biologiques, UMR CNRS 8229, Collège de France, Sorbonne Université, PSL Research University, 75231 Paris Cedex 05, France.

KEYWORDS: polyoxometalates, photocatalysis, CO_2 reduction, DFT calculations, molybdenum(V) phosphate.

ABSTRACT: Three crystalline heterometallic molybdenum(V) phosphates have been synthesized under hydrothermal conditions. They all contain $\{M[P_4Mo_6O_{28}(OH)_3]_2\}^{16-}$ (M = Mn(II) or Co(II)) polyoxometalate (POM) units, with the M ions sandwiched between two $\{P_4Mo^V_6\}$ rings. In the presence of Fe(II) ions in the reaction medium, a 3D **Fe-Mn** compound built from the connection of $Mn(P_4Mo_6)_2$ units to Fe(II) and Fe(III) centers by extra phosphate ions is obtained. Alternatively, the introduction of $[Ru(bpy)_3]^{2+}$ complexes in the synthetic medium prevents the formation of such high dimensional compounds. In the two **Ru(bpy)-Mn** and **Ru(bpy)-Co** hybrids, chains are indeed formed whereby the $Mn(P_4Mo_6)_2$ or $Co(P_4Mo_6)_2$ anions are bridged by Mn(II) or Co(II) ions, respectively. The charge of these anionic chains is compensated by neighboring $[Ru(bpy)_3]^{2+}$ complexes. Among these three compounds, only **Fe-Mn** and **Ru(bpy)-Mn** act as heterogeneous catalysts for the photocatalytic reduction of CO_2 into CH_4 as the major product and CO (yield in CH_4 of 1440 nmol g^{-1} h^{-1} and 600 nmol g^{-1} h^{-1} with a selectivity in CH_4 equal to 92.6 and 85.2%, respectively, under 8 h irradiation) in water, in the presence of TEOA as an electron donor and $[Ru(bpy)_3]^{2+}$ as a photosensitizer. A DFT analysis allowed proposing a reaction mechanism involving the formation of a solvated electron via photoionization of a one-electron reduced $[Ru^{II}(bpy)_2(bpy^{\bullet-})]^+$ complex as the key step to reduce CO_2 to $CO_2^{\bullet-}$. The latter can then coordinate to the peripheral M(II) ions to yield CO through electron and proton transfer steps involving reduced POMs and protons generated in the photooxidation of the sacrificial donor. Concerning the non-active compound, **Ru(bpy)-Co**, DFT calculations revealed that the Co(II) dimers present in the structure may spontaneously take the extra electron out of $CO_2^{\bullet-}$ to form a Co-Co bond, releasing CO_2 back. Finally, preliminary results suggest that the reduction of CO to CH_4 could be photochemically accomplished by the POM-based materials in the presence of TEOA, with no mechanistic requirement for the participation of $[Ru(bpy)_3]^{2+}$.

INTRODUCTION

The photocatalytic reduction of CO_2 to fuels and value-added chemicals (CO, HCOOH, CH_3OH, CH_4…) under sunlight attracts an increasing interest in the context of environmental issues introduced by the shortage of fossil fuels, the need for using solar energy as an alternative and climate change. There is thus an ever-growing incentive to develop efficient, selective and recyclable dedicated heterogeneous catalysts for CO_2 photoreduction reaction (CO_2RR) using visible light. Polyoxometalates (POMs) as soluble anionic metal oxide clusters of d-block transition metals in high oxidation states, typically W(VI), Mo(V,VI) or V(IV,V), exhibit redox and acid-base properties and are particularly exploited in catalysis, either in homogeneous conditions[1,2] or immobilized in solid supports.[3–6] In the hot field of solar energy conversion, although numerous studies have revealed their potentialities as catalysts for water splitting,[7–10] there have been scarce reports on POMs for CO_2RR.[11,12] Besides rare examples of transition metal (M)-substituted polyoxotungstates,[13–16] reduced polyoxomolybdates (*i.e.* containing Mo(V) ions) emerged in 2019 as promising candidates.[17–19] Illustratively, $\{\varepsilon\text{-}Mo^V_{12}Mo^{VI}_4O_{52}\}$ reduces CO_2 into formaldehyde under UV-light in homogeneous conditions[17] and the related $\{\varepsilon\text{-}PMo^V_8Mo^{VI}_4Zn_4O_{52}\}$, as the building unit of a POM-based Metal-Organic Framework (POMOF), selectively reduces CO_2 into formate in heterogeneous conditions under visible light.[18] Two other families of solids made of reduced POM building units have been recently evidenced as heterogeneous photocatalysts for CO_2RR. The $[Co(H_2O)_6]_2[(Mo_2O_4)_8Co_{20}(H_2O)_{28}(HPO_4)_{16}(PO_4)_8(OH)_4]$ solid, which contains large wheels connected by phosphates, Co(II) ions and $\{Mo^V_2O_4\}$ dimers, belongs to the first family and converts CO_2 into CO.[20] The second family gathers crystalline solids based on $\{P_4Mo^V_6\}$ POM units connected by Mn or Co ions which can reduce CO_2 into CO and CH_4 in the presence of $[Ru(bpy)_3]^{2+}$.[19,21,22] Both families

were studied by our group several years ago[23–26] and we decided to revisit their synthesis by adding non-innocent counter-ions such as $[Ru(bpy)_3]^{2+}$ and to investigate their photocatalytic properties for CO_2RR. This strategy was for example explored for POMOFs exhibiting catalytic properties for proton reduction.[27] Another illustrative example is the transformation of the cesium salt of the $[Co_9(H_2O)_6(OH)_3(HPO_4)_2(PW_9O_{34})_3]^{16-}$ POM into the corresponding $[Ru(bpy)_3]^{2+}$ salt.[28] The latter compound was studied as heterogeneous photocatalyst for water oxidation and showed improved performance when compared to that of the cesium salt. The authors proposed that the formation of the photosensitizer-catalyst pair in the solid state is beneficial for the electron transfer event and for the long-term stability of the photosensitizer. In the present study, $[Ru(bpy)_3]^{2+}$ was selected as counter-ion to play the role of photosensitizer although its catalytic role in CO_2RR cannot be excluded as proposed in a number of studies.[20,21,29] We thus report herein the synthesis and structural characterization of three novel heterometallic molybdenum(V) phosphates: **Ru(bpy)-Co** and **Ru(bpy)-Mn** with $\{P_4Mo_6\}$ units linked by Co(II) or Mn(II) ions, respectively, and with $[Ru(bpy)_3]^{2+}$ counter-ions and, as a comparison, the fully-inorganic **Fe-Mn** compound with $\{P_4Mo_6\}$ units connected by Mn(II) and Fe(II) and Fe(III) counter-ions. Only two of these compounds reduce CO_2 into CO and CH_4, and we propose herein a thorough discussion on the relationship between the structures of the reported materials and their photocatalytic properties considering new mechanistic insights provided by DFT calculations.

RESULTS AND DISCUSSION

Synthesis and Characterizations. Hydrothermal synthesis is the method of choice for the preparation of heterometallic molybdenum(V) phosphates. Indeed, these conditions are necessary to promote the reduction of Mo(VI) by metallic Mo to form the $\{Mo^V_2O_4\}$ dinuclear building units. Phosphate ions were added in excess. An acidic pH, between 2 and 4, was also crucial to promote the formation of the molybdenum(V) phosphates. Mixtures of Na_2MoO_4, metallic Mo, concentrated H_3PO_4 and salts of transition metal ions (Fe(II), Co(II), Ni(II) or Mn(II)) in aqueous solution were thus heated at 180°C for 70 h. In addition, $[Ru(bpy)_3]^{2+}$ complexes were introduced in the reaction medium to play the role of counter-ions during the synthesis of **Ru(bpy)-Co** and **Ru(bpy)-Mn**. Finally, following previous observations,[23,26] iminodiacetic acid $[HN(CH_2COO)_2]^{2-}$ was added in the synthesis of **Ru(bpy)-Mn** and **Fe-Mn** to improve their crystallization. All three materials formed dark red crystals, a common feature of compounds containing $\{Mo^V_2O_4\}$ units. Their structure has been solved by single-crystal X-ray diffraction (Table S1). The crystalline homogeneity of the compounds was checked by comparison of the experimental X-ray powder pattern with the powder pattern calculated from the structure solved from single-crystal X-ray diffraction data (Figure S1). The UV-vis spectra of the three compounds (Figure S2) exhibit broad and intense absorption bands. As expected, the UV-vis spectra of **Ru(bpy)-Co** and **Ru(bpy)-Mn** are very close and the broad band at around 450 nm, not present in **Fe-Mn**, can be attributed to MLCT transitions characteristic of the $[Ru(bpy)_3]^{2+}$ complex while the bands common to the three compounds with maxima at around 280 and 510 nm can be attributed to Mo → Mo charge-transfer transitions (*vide infra*). EDX analyses allow to confirm the formula determined by single-crystal analysis for the three compounds (see experimental section). TGA analyses (Figure S3) indicate the number of crystallization water molecules and the comparison of the calculated and experimental mass of oxides formed at high temperature also confirm the proposed formula. The IR spectra of the three compounds (Figure S4) display strong signals consistent with P-O vibrations in the 1000-1150 cm^{-1} region, Mo=O vibrations in the 900-1000 cm^{-1} region and Mo-O vibrations below 800 cm^{-1}. The presence of $[Ru(bpy)_3]^{2+}$ cations in **Ru(bpy)-Mn** and **Ru(bpy)-Co** is confirmed by the comparison of their IR spectra with that of $[Ru(bpy)_3]Cl_2$ showing the presence of characteristic bands (attributed to ν_{C-N} and ν_{C-C} vibrations) between 1350 and 1500 cm^{-1}.

Structure description. The three structures contain the $[(Mo_2O_4)_3(HPO_4)_x(PO_4)_{4-x}(OH)_3]^{(9-x)-}$ (x = 2-3) (P_4Mo_6) anion (Figure 1a). In this anion, three $\{Mo^V_2O_4\}$ dimeric units are connected two by two by sharing edges around a central phosphate group, to form a Mo_6-ring. Three peripheral phosphate groups complete the molecular structure. Valence bond calculations (Figure S5-S7) confirm the +V oxidation state of the Mo ions and indicate that the three oxygen atoms bridging the $\{Mo^V_2O_4\}$ units are protonated. The position of these OH groups is indicated in Figure 1a. Extra protons can also be found on the peripheral phosphate groups. The Mo(V) ions form short Mo-Mo bonds (~2.6 Å) within the dimeric unit. The central and the three peripheral phosphate groups lie in the same side of the plane defined by the six Mo ions. In the three structures, as almost exclusively observed with heterometallic molybdenum(V) phosphates containing P_4Mo_6 anions, the P_4Mo_6 rings are connected in pairs by one metallic ion (Co(II) or Mn(II)) in octahedral coordination, thus forming a sandwich-type, sometimes called "hour-glass", structure (Figure 1b).

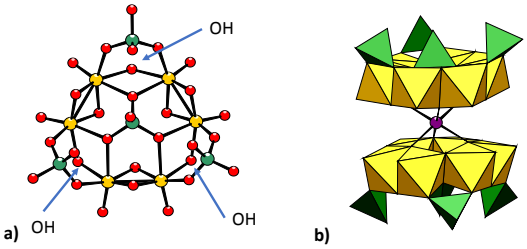

Figure 1. a) Ball and stick representation of the $[(Mo_2O_4)_3(HPO_4)_x(PO_4)_{4-x}(OH)_3]^{(9-x)-}$ (P_4Mo_6) anion with the indication of the protonated bridging oxygen atoms and b) polyhedral representation of the sandwich-type structure formed by the connection of two P_4Mo_6 anions by a Co(II) or Mn(II) ion in octahedral coordination. Yellow octahedra: MoO_6, green tetrahedra: PO_4, yellow spheres: Mo, red spheres: O, green spheres: P, purple sphere: M (M = Co or Mn).

In the structure of **Ru(bpy)-Co** (Figure 2a, left) two P_4Mo_6 rings are sandwiched by a Co(II) ion (Co1). These sandwich-type POMs are connected to each other by dimers of Co(II) ions to form a 1D chain. Co2 and Co3 adopt a distorted octahedral coordination, being connected to three oxygen atoms of phosphate ions, two terminal water ligands and one

bridging water molecule (Figure S8a). The Co2-Co3 distance is quite short (2.91 Å) within a Co(II) dimer. The charge of the anionic chains is compensated by neighboring $[Ru(bpy)_3]^{2+}$ counter-ions (Figures 2b, left).

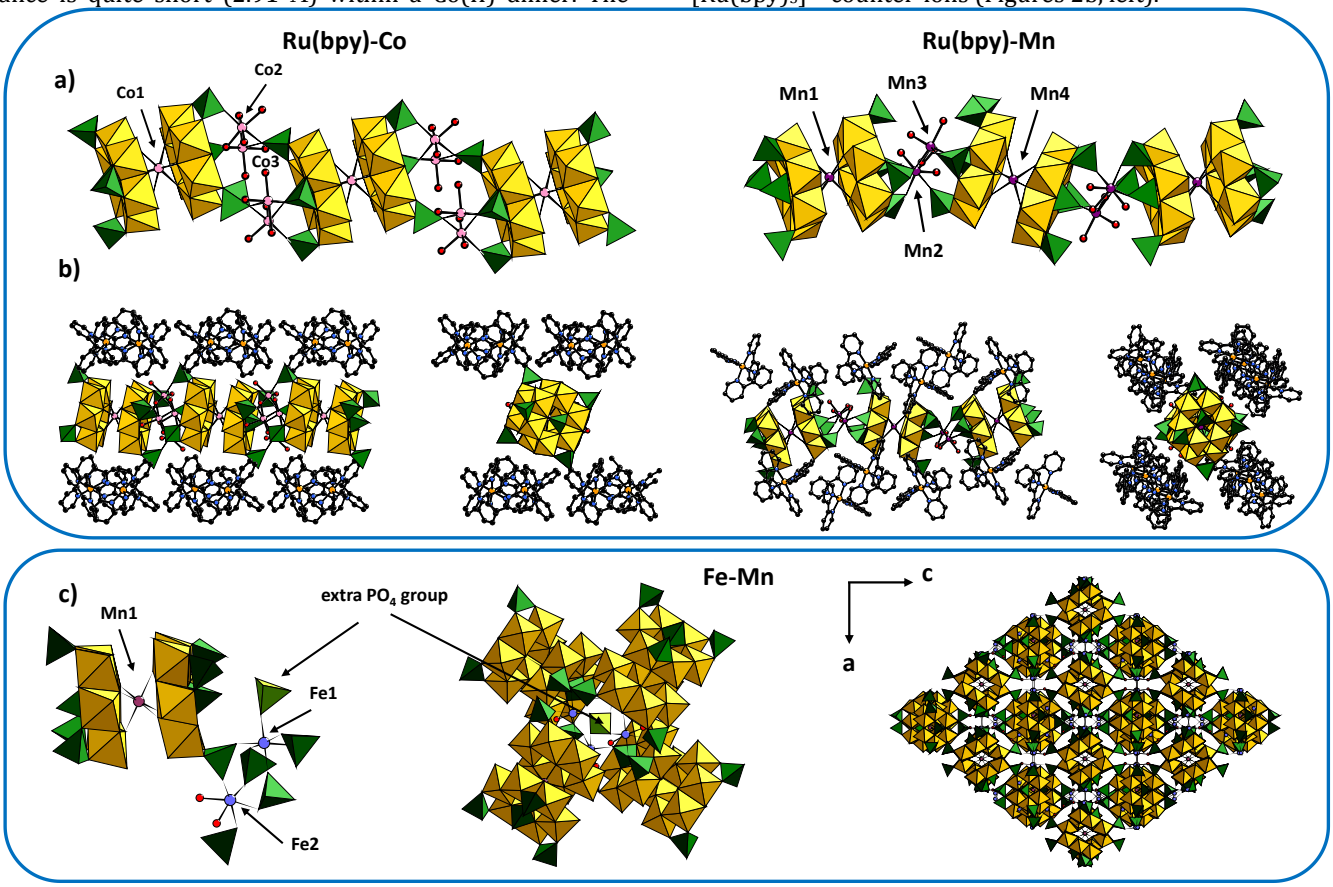

Figure 2. a) View of the chain formed by the connection of $M(P_4Mo_6)_2$ sandwich-type POMs by M(II) ions in the structures of **Ru(bpy)-M** (M = Co, Mn), b) side view (left) and top view (right) of the chains surrounded by $[Ru(bpy)_3]^{2+}$ cations in each structure; c) view of the structural unit in **Fe-Mn**, which consists in a $Mn(P_4Mo_6)_2$ sandwich-type anion, one Fe(III) ion (Fe1), one Fe(II) ion (Fe2) and one extra PO_4 group (left); view of the extra PO_4 group bound to four $Mn(P_4Mo_6)$ sandwich-type anions via Fe-O(PO_3) bounds (middle); view along the *b* axis of the 3D structure (right). Yellow octahedra : MoO_6, green tetrahedra : PO_4, red spheres : O, purple spheres : Mn, pink spheres: Co, blue spheres: Fe, orange spheres: Ru, black spheres: C, dark blue spheres: N; hydrogen and sodium atoms have been omitted for clarity.

The structure of **Ru(bpy)-Mn** has similarities with that of **Ru(bpy)-Co**, with Mn(II) ions replacing Co(II) ions (Figure 2a, right). However, the two compounds are not isostructural and present some differences. In **Ru(bpy)-Mn**, there are two inequivalent independent P_4Mo_6 rings with two inequivalent Mn(II) ions (Mn1 and Mn4) connecting them (Figure 2a). These $Mn(P_4Mo_6)_2$ sandwich-type ions stack into chains like in the $Co(P_4Mo_6)_2$ analogue in **Ru(bpy)-Co**. Still, while these entities
are stacked in a parallel fashion within a chain in **Ru(bpy)-Co**, the chain in **Ru(bpy)-Mn** adopts a zig-zag shape with tilted anionic units. Furthermore, the POMs are connected by four Co(II) ions in **Ru(bpy)-Co** while only two Mn(II) ions link the anionic entities in **Ru(bpy)-Mn**. Mn2 and Mn3 are in a pseudo-octahedral coordination environment, being connected to three water ligands and to three oxygen atoms of phosphate ions (Figure S8b). In addition, in contrast to what is observed in the structure of the Co analogue, the two Mn ions are not directly connected via an oxygen atom of a bridging water molecule but are separated by a sodium ion (Figure S8b). $[Ru(bpy)_3]^{2+}$ counter-ions are intercalated between the chains (Figures 2b). Finally, **Fe-Mn** does not contain additional transition metal complexes as counter-ions as in the two other structures reported herein but is a fully inorganic structure with P_4Mo_6 rings sandwiched by a Mn(II) ion (Mn1) and further linked by Fe ions. Its structure is reminiscent of that of the previously reported molybdenum(V) phosphates, namely $Na_{15}Mn_{10}[(Mo_2O_4)_3(HPO_4)(PO_4)_3(OH)_3]_4(PO_4)$,[26] $Na_7Mn_4Fe_6[(Mo_2O_4)_3(HPO_4)_2(PO_4)_2(OH)_3]_4(PO_4)$,[23] NENU-605[19] and NENU-606[19], which all crystallize in the tetragonal $I4_1/acd$ space group and contain $Mn(P_4Mo_6)_2$ sandwich-type units. One additional common feature between these structures is the presence of an extra phosphate ion which does not belong to a P_4Mo_6 ring. The difference between them lies in the nature of the transition metal ions connecting these rings. In **Fe-Mn**, the $Mn(P_4Mo_6)_2$ sandwich-type units are connected to each other and to the extra phosphate group via Fe(II) and Fe(III) ions (Figure 2c). BVS calculations unambiguously allowed to determine that Fe1 is a Fe(III) ion while Fe2 is in the +II oxidation state (Figure S7), Fe1 and Fe2 being both in octahedral environments. Fe1 is coordinated to six oxygen atoms of phosphate groups and Fe2 is bound to four oxygen atoms of phosphate groups of

P_4Mo_6 units and to two water molecules (Figure S8c). The four oxygen atoms of the extra PO_4 group are bound to Fe1 ions. Overall, the connection of the POMs via these Fe-O(PO_3) bonds generates a compact 3D structure (Figure 2c). Still, the presence of Fe(III) in **Fe-Mn** can be unexpected since the synthesis of reduced molybdenum phosphates requires a strong reducing environment and the iron source used is a Fe(II) salt. In order to validate the BVS calculations, XPS analyses were conducted on **Fe-Mn**. Figure S9 shows the XPS survey obtained on this compound. Surface analysis reveals the presence of all the constitutive elements of the POM-based material. The Fe2p spectral region presented in Figure 3 clearly shows broad peaks centered at 712.0 and 725.1 eV attributed to $Fe2p_{3/2}$ and $Fe2p_{1/2}$, respectively. Their asymmetric shape reveals the presence of at least two different chemical environments for Fe. Instead of fitting the experimental data by the classical deconvolution with Gaussian/Lorentzian mix parameters, an original approach was adopted here to reconstruct the Fe2p doublet whereby a linear combination of Fe(II) (green line) and Fe(III) (red line) reference spectra was used. The orange line represents the obtained envelope. This non-linear least-squares fitting allowed determining the amount of each oxidation state. The XPS ratio thus obtained is 1:1 (precisely 49% Fe(II) and 51% Fe(III)) which is in perfect agreement with BVS.

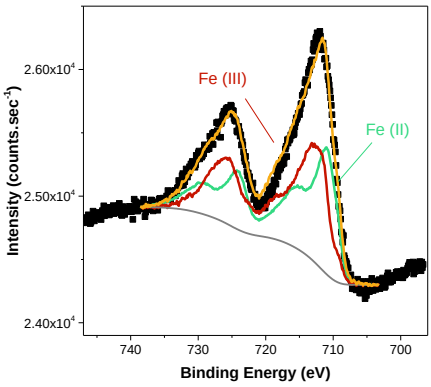

Figure 3. Fe2p spectral region recorded on the **Fe-Mn** compound (black squares) and its reconstruction (orange line) from a linear combination of Fe(II) (green line) and Fe(III) (red line) reference spectra acquired in the same experimental conditions.

Photocatalytic properties. The photocatalytic properties of the three compounds were studied in aqueous suspensions of ground crystals, with triethanolamine (TEOA) as the electron donor (H_2O/TEOA = 14:1). Despite the presence of $[Ru(bpy)_3]^{2+}$ entities in the framework of **Ru(bpy)-Co** and **Ru(bpy)-Mn**, no gaseous products nor formate in the liquid phase were detected under visible light irradiation. However, in the presence of additional photosensitizer $[Ru(bpy)_3]Cl_2$ dissolved in the catalytic medium, the formation of CO and CH_4 could be observed in the gas phase for two of the three compounds, **Ru(bpy)-Mn** and **Fe-Mn**, with no formate production. For these two compounds, CH_4 was the major product detected and its production increased almost linearly with the irradiation time (Figure 4). In contrast, the production of CO was much lower and stopped after a few hours. The CH_4 production amounts to 48.0 nmol (i.e. 600 nmol g^{-1} h^{-1}) and 115.2 nmol (i.e. 1440 nmol g^{-1} h^{-1}) after 8 h, with selectivities of 85.2% and 92.6% for **Ru(bpy)-Mn** and **Fe-Mn**, respectively. **Fe-Mn** is thus the most efficient catalyst, with an activity for CH_4 production comparable to that observed for the related fully-inorganic P_4Mo_6-based heterometallic molybdenum(V) compounds NENU-605 (894.7 nmol g^{-1} h^{-1}) and NENU-606 (1747.8 nmol g^{-1} h^{-1}) studied in similar conditions.[19] However, the selectivity of **Fe-Mn** for CH_4 (92.6%) is better than the selectivity of these two compounds (76.6% and 85.5% for NENU-605 and NENU-606, respectively). Furthermore **Ru(bpy)-Mn** does not show any deactivation for CH_4 production even after 48 h (Figure S10) while a plateau was observed after 24 h for both NENU-605 and NENU-606. Moreover, IR spectra and X-ray powder patterns of **Ru(bpy)-Mn** and **Fe-Mn** before and after catalysis are quite similar (Figures S11 and S12), confirming the stability of these materials under photocatalytic conditions. Finally, only a small loss of activity was observed after 3 consecutive catalytic assays for the **Ru(bpy)-Mn** catalyst (Figure 4d).

Mechanistic study. Next, we conducted DFT calculations to shed light onto the mechanism responsible for the CO_2RR and to rationalize the experimentally observed reactivity trends. Owing to the presence of *d* electrons in fully-reduced POMs such as $\{P_4Mo^V_6\}$, it was initially postulated that POMs may be able to transfer electrons to interstitial metal centers under light irradiation to generate a M(I) ion where a CO_2 molecule could be then reduced upon coordination.[19,22] In such a scenario, a photoexcited (or photoreduced) form of $[Ru(bpy)_3]^{2+}$ would allow regenerating the fully-reduced POM complex with the help of a sacrificial electron donor. More recently, photophysical studies suggested that the CO_2RR is attained by the photoexcited $[Ru(bpy)_3]^{2+}$ complex rather than by $\{P_4Mo^V_6\}$-containing materials, as the presence of CO_2 induces a faster decay of the transient photovoltage of $[Ru(bpy)_3]^{2+}$, whereas that of $\{P_4Mo^V_6\}$-based crystals is not significantly altered.[20] Similar findings were also reported for larger Mo(V)-phosphate POMs.[19]

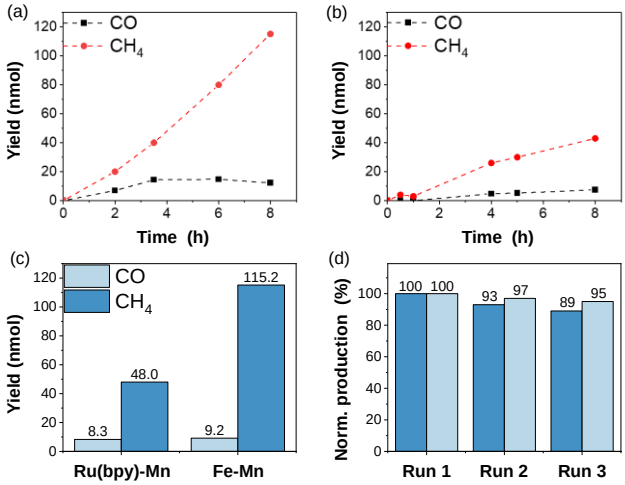

Figure 4. CO_2 photoreduction toward CO and CH_4 with a)

Fe-Mn and b) **Ru(bpy)-Mn** catalysts; c) comparison of the production of the two compounds after 8 h; d) Recyclability experiments with **Ru(bpy)-Mn**. Light and dark blue bars indicate CO and CH_4 production, respectively. The catalyst was collected by centrifugation after 8 h then washed after each catalytic assay. Reactions conditions: 10 mg of compound, 30 mL H_2O/TEOA (14:1), 0.01 mmol $[Ru(bpy)_3]Cl_2$, 280 W Xe lamp, $\lambda > 415$ nm.

Firstly, we analyzed the electronic structure of the materials as well as their photochemical properties. To do so, we selected the catalytically active **Ru(bpy)-Mn** as a representative example due to its 1D nature which facilitates the modeling of the crystal-solvent interphase where reactivity takes place. Previous computational studies have shown that the reduction of CO_2 to CO requires the coordination of CO_2 to an active metal center through the carbon atom to induce the charge transfer from an electron-rich ligand or from the metal itself to form a M-$COO^{\bullet-}$ intermediate.[30–38] In our system, the phosphate-coordinated Mn2 and Mn3 metals (as labelled in Figure 2a) bearing labile aqua ligands, thus with potential as coordination sites for binding CO_2, are more likely to participate in the reaction mechanism compared to those sandwiched between two $\{P_4Mo_6\}$ rings, *i.e.* Mn1 and Mn 4 (as labelled in Figure 2a), which are hexacoordinated by bridging oxygens of the POM. We thus performed our study using the model system depicted in Figure 5a. This model consists of two $\{P_4Mo_6\}$ rings belonging to two different sandwich units, the two phosphate-coordinated Mn(II) ions (Mn2 and Mn3) and a Na^+ counter ion, while using closed-shell $Zn(II)(OH_2)_3$ as capping groups in place of Mn1 and Mn4. The $\{P_4Mo_6\}$ clusters were described as closed-shell singlets, the six d(Mo) electrons being localized in three Mo—Mo bonds, whereas Mn(II) ions are stabilized in their high-spin state, bearing five unpaired electrons each.

The density of states (DOS) (Figure 5b) shows that both the HOMO and the LUMO are centered in POM units, whilst virtual and occupied orbitals with Mn contribution (yellow curve in Figure 5b) are separated by a wider energy gap, in such a way that the most stable Mn-centered virtual MO lies ca. 2 eV above the LUMO. TD-DFT calculations (Figures S15-17 and derived text in the SI) revealed that the electronic transitions accessible in the visible region involve the highest set of occupied MOs of σ(Mo-Mo) character and the first two sets of virtual MOs, which are antibonding combinations of d(Mo) and p(O) orbitals (Figure 5b), typical of POM structures.[39] Thus, the photogeneration of a Mn(I) species via internal charge transfer within the crystal is unlikely (see SI for more details). Likewise, the photoreduction of Mn(II) centers by photoactivated $[Ru(bpy)_3]^{2+}$ counterions was found to be unlikely as well (*vide infra*).

To further investigate the processes that may occur when irradiating such a complex multi-component system, we evaluated the feasibility of possible interactions between the POMs, the Ru complex and the TEOA sacrificial donor. On the one hand, $[Ru(bpy)_3]^{2+}$ is well-known to undergo a metal-to-ligand charge transfer (MLCT) upon visible-light absorption, leading to a singlet MLCT state that rapidly evolves towards a long-lived triplet MLCT state, $^3[Ru^{III}(bpy)_2(bpy^{\bullet-})]^{2+,*}$, via intersystem crossing (ISC).[40] On the other hand, the $\{P_4Mo_6\}$ POMs can also interact with visible light, leading to internal transitions of metal-centered (MC) and metal-to-metal charge transfer (MMCT) character that involve the Mo(V) ions of the cluster (Figures S3 and S15). As predicted by our DFT calculations, the HOMOs of both the POM and the $[Ru(bpy)_3]^{2+}$ lie below in energy that of TEOA sacrificial donor (Figure 5c) suggesting that both systems are susceptible of generating, upon absorbing a photon, a hole at a suitable energy level to be quenched by TEOA, in agreement with previous measurements.[20] It is worth mentioning that the one-electron reduced POM containing one Mo(IV) center, namely POM(1e) in Figure 5c, could also reduce the ^{3}MLCT state of $[Ru(bpy)_3]^{2+}$ (ΔG = -43.1 kcal·mol^{-1}), whereas this reductive quenching is not favorable when using the parent, all Mo^V-POM cluster as electron donor (ΔG = +8.2 kcal·mol^{-1}). Also, the $^3[Ru^{III}(bpy)_2(bpy^{\bullet-})]^{2+,*}$ excited state is not reducing enough to spontaneously transfer an electron to the ground state of the POM (ΔG = +7.9 kcal·mol^{-1}), although an excited state of the POM may reduce $[Ru(bpy)_3]^{2+}$, as the LUMO of $[Ru(bpy)_3]^{2+}$ is slightly lower in energy than that of the POM (Figure 5c). Overall, this analysis indicates that the Ru complex is the species that acts as electron acceptor, while the $\{P_4Mo_6\}$ clusters in the crystal could act as electron shuttles, facilitating a formal electron transfer from TEOA to $[Ru(bpy)_3]^{2+}$ upon irradiation.

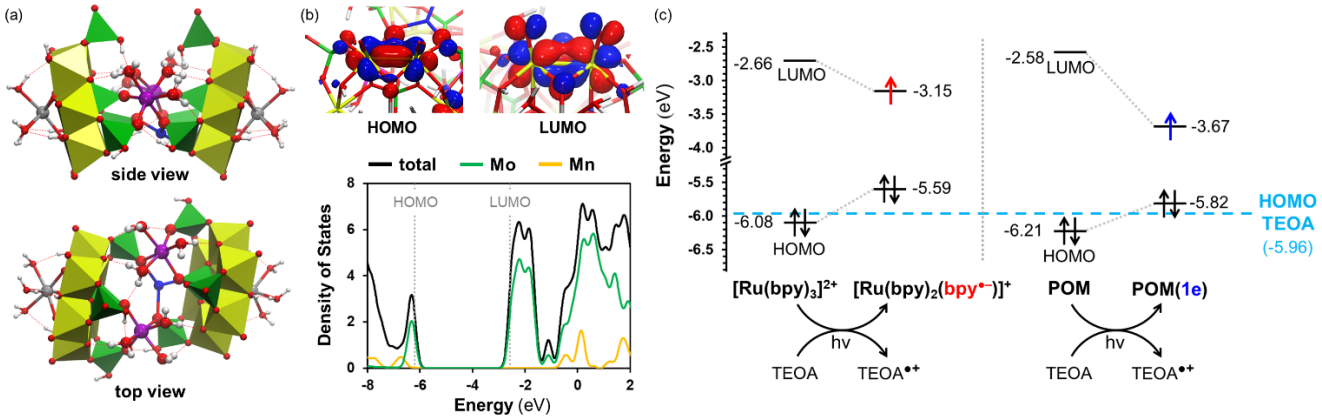

Figure 5. a) Two views of the B3LYP-optimized structure for the model of **Ru(bpy)-Mn**. Color code: Mn (purple), Mo (yellow), P (green), Na (blue), O (red), H (white), capping Zn (silver), b) Density of states (DOS) obtained from the model system accompanied by isovalue representations of the frontier MOs (see Figure S13 for comparison with other methods and Figure S14 for a spin density representation). A Gaussian broadening function with a full width at half maximum of 0.3 eV is displayed for clarity (see Computational Details section for further details). The black curve represents the total DOS, while green and orange curves represent the projected DOS for Mo and Mn, respectively, c) Frontier MO diagram comparing the energy levels of $[Ru(bpy)_3]^{2+}$, POM clusters within the **Ru(bpy)-Mn** model; and their one-electron reduced counterparts: $[Ru(bpy)_2(bpy^{\bullet-})]^{+}$ and POM(1e), which contains one $\{P_4Mo^{IV}Mo^{V}_5\}$ unit. The energy level of the HOMO of TEOA is represented with a blue dashed line.

Determining the free energy variation associated to the reductive quenching of the photoexcited POM is rather complex due to the large number of states that may be formed and involved in the relaxation pathway. Nevertheless, the step-wise quenching of $^3[Ru^{III}(bpy)_2(bpy^{\bullet-})]^{2+,*}$ by TEOA has been estimated to be exergonic by 5.4 kcal·mol^{-1}: in a first step, the reduction of the ^{3}MLCT generates a TEOA$^{\bullet+}$ species in a slightly endergonic process (by 1.6 kcal·mol^{-1}), which is followed by the rapid decomposition of the latter via interacting with a second TEOA molecule to yield a neutral TEOA$^{\bullet}$ plus a protonated HTEOA$^+$.[41–43] This second step is exergonic by 7 kcal·mol^{-1} in water and gives the thermodynamic driving force to the quenching process.

The gained knowledge about the charge-transfer processes underlying to the $\{P_4Mo_6\}/[Ru(bpy)_3]^{2+}$ photosystem prompted us to propose a novel mechanism for the reduction of CO_2 to CO, in which $[Ru(bpy)_3]^{2+}$ acts as the catalyst and the POM-based material as a co-catalyst. This mechanistic proposal is represented in Figure 6 and further evaluated by means of theoretical and experimental approaches.

Firstly, the formation of the POM(1e) and the $[Ru^{II}(bpy)_2(bpy^{\bullet-})]^+$ species (highlighted in yellow and green in Figure 6, respectively) occurs photochemically as described above. Although these are electron-rich species, they cannot accomplish the reduction of CO_2. The direct reduction of CO_2 on the Mn(II) center of POM(1e) to give the POM-Mn^{II}-COO$^{\bullet-}$ intermediate species is prohibitively costly, with a ΔG of +32.6 kcal·mol^{-1}, whereas the redox potential of the $[Ru^{II}(bpy)_3]^{2+}/[Ru^{II}(bpy)_2(bpy^{\bullet-})]^+$ pair (-1.50 V *vs* SCE)[44] is 0.65 V less negative than that of $CO_2/CO_2^{\bullet-}$ (-2.15 V *vs* SCE).[45] However, the absorption of a photon by $[Ru^{II}(bpy)_2(bpy^{\bullet-})]^+$ could promote its photoionization via a *ligand-to-solvent charge transfer* (LSCT), generically known as *charge transfer to solvent* (CTTS), to regenerate the $[Ru^{II}(bpy)_3]^{2+}$ species yielding a solvated electron (e^-_{aq}). In the presence of CO_2, solvated electrons tend to localize in an empty π* MO of CO_2, resulting in a $CO_2^{\bullet-}$ radical anion with a bent structure[46,47] and importantly, accomplishing the first electron injection. The photoionization of $^3[Ru^{III}(bpy)_2(bpy^{\bullet-})]^{2+,*}$ has been reported for wavelengths that range from the UV[48] to the violet[49] regions of the spectrum. Thus, it might be reasonable to think that the LSCT band that originates from the ground state of $[Ru^{II}(bpy)_2(bpy^{\bullet-})]^+$ (which bears a lower positive charge) is red-shifted due to the higher-lying nature of the SOMO (Figure S18), favoring the photogeneration of solvated electrons at our photocatalytic conditions (λ > 415 nm).

The $CO_2^{\bullet-}$ generated in solution coordinates through its C atom to a Mn(II) center of the **Ru(bpy)-Mn** crystal replacing a labile aqua ligand. This endergonic process (+14.2 kcal·mol^{-1}) generates a Mn-COO$^{\bullet-}$ intermediate that can then take a proton from a HTEOA$^+$ molecule through a rapid process whereby one electron from a POM(1e) cluster of the material is spontaneously transferred to the CO_2 moiety to yield a Mn^{II}-COOH species. This step was estimated to be barrierless in terms of Gibbs free energy, with a very smooth electronic, potential energy barrier of 2.9 kcal·mol^{-1}. The transition state (TS) for this concerted proton and electron transfer is represented in Figure S19. Alternatively, this process may also take place using TEOA$^{\bullet}$ as both proton and electron donor, transferring a formal H$^{\bullet}$ to the Mn-COO$^{\bullet-}$ intermediate as shown in Scheme S1. The Mn^{II}-COOH intermediate lies 7.1 kcal·mol^{-1} above the Mn-aqua reactant and, as shown in Figure S20, the localization of a formal negative charge on the C atom directly bound to Mn results in the decoordination of one of the phosphate oxygens from the coordination sphere of Mn, presumably due to Pauling repulsion.

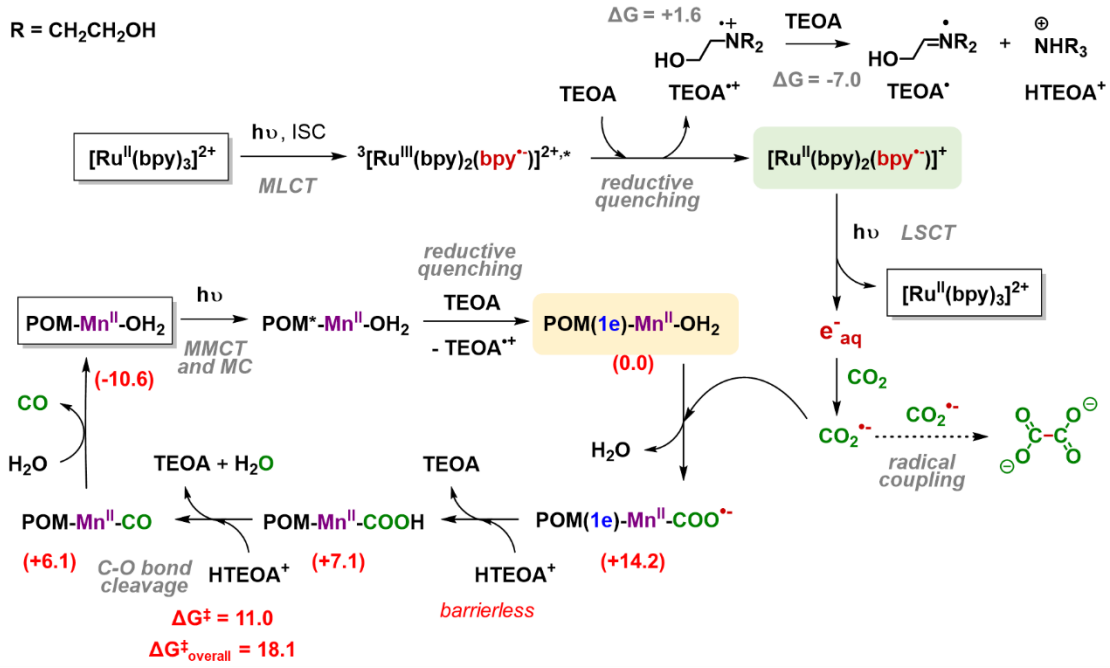

Figure 6. Proposed mechanism for the photoreduction of CO_2 to CO catalyzed by $[Ru(bpy)_3]/\{P_4Mo_6\}$ systems using TEOA as sacrificial donor. Gibbs free energies are given in kcal·mol^{-1}. Values in parentheses indicate relative Gibbs free energies. MLCT, ISC, MMCT, MC and LSCT stand for *metal-to-ligand* charge transfer, intersystem crossing, *metal-to-metal* charge transfer, *metal-centered* and *ligand-to-solvent* charge transfer, respectively.

Finally, the protonation of the Mn-COOH species by a second $HTEOA^+$ molecule promotes the cleavage of the C—O(H) bond. This process occurs through the concerted TS represented in Figure 7, which is the point of highest energy in the free-energy pathway describing the thermally-activated reduction of $CO_2^{\bullet-}$ to CO, accounting for an overall free energy barrier of 18.1 kcal·mol^{-1} that can be easily overcome at room temperature. Note that due to the protic nature of the solvent (water) it cannot be discarded that protons migrate from $HTEOA^+$ to the catalytic sites through water molecules acting as proton shuttles. The C-O bond scission releases a water molecule and leads to the CO product coordinated to a six-fold coordinated Mn(II) center. This species is slightly more stable than the Mn-COOH intermediate (by 1 kcal·mol^{-1}) but it is not until the CO product is released to the solution, being replaced by a water molecule to regenerate the Mn-OH_2 species, that the whole process becomes irreversible, with a reverse free-energy barrier of almost 29 kcal·mol^{-1}. It is worth noting that the formation of a Mn(II) hydride intermediate is prohibitively endergonic (see Scheme S2), being thus consistent with the absence of $HCOO^-$ and H_2 products reported experimentally. This suggests that the nature of the interstitial metal centers in the material is a paramount factor governing the product selectivity.

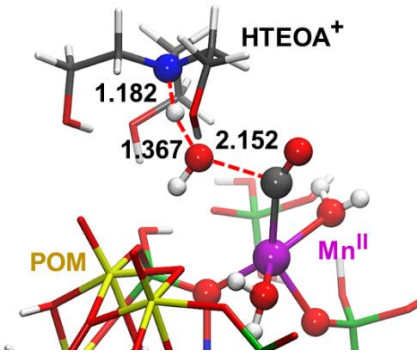

Figure 7. Optimized geometry of the transition state for the key C—O bond cleavage step. Main distances are given in Å.

Aside from evolving to CO on the crystal surface, we can envisage an alternative pathway whereby $CO_2^{\bullet-}$ may undergo a radical coupling with another $CO_2^{\bullet-}$ ion to form an oxalate anion ($C_2O_4^{2-}$), which may prevail in the absence of coordination sites. In view of this possible route, we reperformed blank experiments in the absence of POM-based crystals, not only verifying the absence of CO and CH_4, but more importantly revealing the formation of oxalate anions as demonstrated by ^{13}C NMR (Figures S21 and S22) and also confirmed by IC measurements, thus supporting the generation of $CO_2^{\bullet-}$ anions in solution by the Ru complex. Furthermore, this also evidences that $[Ru^{II}(bpy)_3]^{2+}$ alone is not sufficient for yielding CO and thus, in absence of metal centers where $CO_2^{\bullet-}$ can bind to carry on with the reaction, the generated $CO_2^{\bullet-}$ ions dimerize via radical-radical coupling to form oxalate, which is fully consistent with the proposed reaction mechanism and the roles of the Ru complex and the POM crystal as catalyst and co-catalyst, respectively.

Next, we sought to understand why despite being structurally similar, the **Ru(bpy)-Mn** (active) and **Ru(bpy)-Co** (inactive) lead to remarkably distinct catalytic activities. Experimental UV-Vis spectra (Figure S5) already anticipated that the photochemical properties of both materials are rather alike, in agreement with the similar energy levels obtained for the $\{P_4Mo_6\}$ clusters in both systems (Figures S23 and S24). Thus, the nature of the POM-material should not alter the ability of the Ru complex to reduce CO_2 to $CO_2^{\bullet-}$. This strongly support that the peripheral Mn(II) centers in the **Ru(bpy)-Mn** crystal participate explicitly in the reaction mechanism, in line with the mechanism proposed in Figure 5, playing a critical role that the Co(II) centers in **Ru(bpy)-Co** cannot. Indeed, analysis of the key coordination step of $CO_2^{\bullet-}$ to Co(II) centers **Ru(bpy)-Co** revealed that, unlike Mn(II) centers in **Ru(bpy)-Mn** and Fe(II) centers of the also catalytically active **Fe-Mn** (Figure S25), Co(II) ions *cannot* stabilize a M-$COO^{\bullet-}$ intermediate. Instead, $\{Co(II)\}_2$ dimers act as an electron sink taking the extra electron from the $CO_2^{\bullet-}$ fragment to form a Co-Co bond and regenerate CO_2. This can be explained by the fact that virtual Co-centered orbitals are deeper in energy than those of Mn (Figure S24), being more easily filled by a reducing agent, here the $CO_2^{\bullet-}$ anion. The difference between Mn(II)- and Co(II)-containing materials is illustrated in Figure S26 by means of simple model systems. Importantly, the lack of CO/CH_4 products reported for **Ru(bpy)-Co** can be explained through its inability to coordinate and stabilize a reduced CO_2 molecule, further supporting our mechanistic proposal.

Finally, we attempted to propose a plausible mechanism to explain the subsequent reduction of CO to CH_4. Very recently, we have characterized the TEOA$^\bullet$ species, which originates from the oxidation of TEOA, as a hydride-donor that is capable of hydrogenating a Lewis-acid activated CO_2 molecule to formic acid (unpublished results). A preliminary analysis of the reaction profile involved in the present case suggests that CO could bind to Mn(II) sites and be reduced to formaldehyde, then to methanol and finally to methane via sequential hydride-transfer steps from the allylic carbon of TEOA$^\bullet$ to the carbon atom of the substrate and protonation steps (Figure S28 and Table S2). According to this, homogeneous $[Ru(bpy)_3]^{2+}$ would not be strictly required for the reduction of any of these intermediates to methane. Indeed, additional catalytic experiments showed that in aqueous solutions with TEOA and in the absence of $[Ru(bpy)_3]^{2+}$, **Ru(bpy)-Mn** is capable of reducing methanol to methane by itself under light irradiation (Figure S29). Nonetheless, the yield of CH_4 increases significantly when homogeneous $[Ru(bpy)_3]^{2+}$ is added to the reaction mixture, most likely due to an enhanced photooxidation of TEOA caused by the electron flow from reduced POMs to $[Ru(bpy)_3]^{2+}$ and by the role of the latter as an additional TEOA photo-oxidant. Although these facts are consistent with TEOA$^\bullet$ being related with the CO reduction to CH_4, further experimental and theoretical analyses are required to fully understand this process.

CONCLUSION

Three novel structures containing the $\{P_4Mo_6\}$ anionic building unit connected by first-row transition metal ions were successfully isolated by hydrothermal synthesis. **Ru(bpy)-Co** and **Ru(bpy)-Mn** exhibit a 1D structure with $M(P_4Mo_6)_2$ (M = Co or Mn) sandwich-type POMs connected by additional Co(II) or Mn(II) ions. Conversely, **Fe-Mn** does not contain additional transition metal complexes and the POM units are interconnected via Fe-O(PO_3) bonds, forming a compact 3D structure. Notably, **Ru(bpy)-Mn** and **Fe-Mn** can reduce CO_2 into CH_4 and CO under visible light in the presence of additional $[Ru(bpy)_3]^{2+}$ complexes added to the solution; whereas **Ru(bpy)-Co** was found to be inactive. **Fe-Mn** exhibits a remarkable selectivity of CO_2 to CH_4 conversion up to 92.6% and **Ru(bpy)-Mn** does not show any deactivation even after 48 h. The lack of catalytic activity of the cobalt-containing **Ru(bpy)-Co** compound indicates that the sole combination of electron-rich POM units and first-row transition metal ions is not sufficient to lead to active materials for CO_2RR and that their composition and crystalline assembly is crucial.

The analysis of the electronic structure and photochemical properties of the different species by means of DFT allowed proposing a novel mechanism to explain the photoreduction of CO_2 promoted by these multi-component catalytic systems. Firstly, DFT calculations revealed that both the $\{P_4Mo_6\}$ units and the $[Ru(bpy)_3]^{2+}$ present in solution can photo-oxidize the TEOA sacrificial donor. The $[Ru(bpy)_3]^{2+}$ complex is proposed to act as the catalyst, since its one-electron reduced form, *i.e.* $[Ru^{II}(bpy)_2(bpy^{\bullet-})]^+$, can undergo photo-ionization to form a solvated electron, which can then reduce a CO_2 molecule to form a $CO_2^{\bullet-}$ anion in solution. The latter can bind to metal sites with labile ligands and weak oxidizing character such as Mn(II) ions in **Ru(bpy)-Mn** to be further reduced by reduced POMs in the material and protonated to generate a Mn-COOH intermediate, which can evolve toward the Mn-coordinated CO product via protonation and C—O(H) bond cleavage, releasing a water molecule. However, in the absence of accessible metal sites, the formation of CO is blocked and $CO_2^{\bullet-}$ ions couple to form oxalate, highlighting the role of the POM as co-catalyst. Remarkably, this proposal is consistent with a series of key experimental facts: i) $[Ru(bpy)_3]^{2+}$ can photo-reduce CO_2 only to oxalate in the absence of POM crystals; ii) POM crystals do not form any reduction product without $[Ru(bpy)_3]^{2+}$ but their combination divert the product from oxalate to CO (and CH_4); iii) **Ru(bpy)-Co** does not yield CO because the $\{Co(II)\}_2$ dimers spontaneously reoxidize $CO_2^{\bullet-}$ to CO_2 upon binding.

Overall, this study further evidences that the heterometallic molybdenum(V) phosphates can be used to build up stable multi-component catalytic systems for the photocatalytic reduction of CO_2 into the high-valued CH_4 hydrocarbon with high selectivity. Moreover, it provides insights into the complex mechanism governing the reaction mechanism at an atomic level, which might serve for designing the next generation of more efficient CO_2RR catalysts.

EXPERIMENTAL SECTION

Synthesis and Characterizations. All reagents were purchased from commercial sources and used as received. Molybdenum powder 1-5 μm with purity >99.9% was used for the synthesis. $[Ru(bpy)_3]Cl_2{\cdot}6H_2O$was synthesized according to reported procedures.[50] Hydrothermal syntheses were carried out in 23 mL polytetrafluoroethylene lined stainless steel containers under autogenous pressure. All reactants were briefly stirred before heating. The mixture was heated to 180 °C over a period of 1 h, kept at 180 °C for 70 h and cooled down to room temperature over a period of 20 h. The pH mixture was measured before (pH_i) and after the reaction (pH_f). The product was isolated by filtration after sonication and washed with ethanol.

Preparation of $[Ru(bpy)_3]_2Co^{II}_5[P_4Mo_6O_{26}(OH)_5]_2{\cdot}22H_2O$ (**Ru(bpy)-Co**): A mixture of $Na_2MoO_4{\cdot}2H_2O$ (0.235 g, 0.98 mmol), metallic Mo (0.030 g, 0.31 mmol), concentrated (85 wt%) H_3PO_4 (73 μL, 1.11 mmol), $CoCl_2{\cdot}6H_2O$ (0.420 g, 1.76 mmol), $[Ru(bpy)_3]Cl_2.6H_2O$ (0.200 g, 0.27 mmol) and H_2O (4 mL) was stirred and the pH was adjusted to 2.0 with 4 M HCl (pH_f = 2.0). Red crystals were isolated after filtration and sonication in ethanol (0.067 g, 14.7 % based on Mo). Metal composition was checked by EDX analysis: P/Mo = 0.55 (calc 0.67); Ru/P = 0.29 (calc 0.25); Co/P = 0.70 (calc 0.62). IR (ν/cm^{-1}): 1624 (w), 1601 (w), 1460 (w), 1441 (w), 1421 (w), 1310 (m), 1166 (w), 1122 (w), 1060 (m), 1001 (s), 959 (s), 926 (s), 882 (s), 769 (m), 729 (m), 677 (m), 608 (w), 530 (m).

Preparation of $Na_2[Ru(bpy)_3]_2Mn^{II}_3[P_4Mo_6O_{25}(OH)_6]_2{\cdot}20H_2O$ (**Ru(bpy)-Mn**): A mixture of $Na_2MoO_4{\cdot}2H_2O$ (0.470 g, 1.95 mmol), metallic Mo (0.030 g, 0.31 mmol), concentrated (85 wt%) H_3PO_4 (290 μL, 4.42 mmol), $NiCl_2{\cdot}6H_2O$ (0.148 g, 0.622 mmol), $MnCl_2{\cdot}4H_2O$ (0.119 g, 0.59 mmol), iminodiacetic acid (0.100 g, 0.75 mmol), $[Ru(bpy)_3]Cl_2.6H_2O$ (0.100 g, 0.13 mmol) and H_2O (4 mL) was stirred and the pH was adjusted to 2.5 with 4 M HCl (pH_f = 2.5). Red crystals were isolated after filtration and sonication in ethanol (0.065 g, 8.8 % based on Mo). Metal composition was checked by EDX analysis: P/Mo = 0.61 (calc 0.67); Ru/P = 0.30 (calc 0.25); Mn/P = 0.30 (calc 0.37); Na/P = 0.17 (calc. 0.25). IR (ν/cm^{-1}): 1634 (w), 1600 (w), 1464 (w), 1441 (w), 1421 (w), 1118 (m), 1001 (s), 958 (s), 923 (s), 768 (m), 726 (s), 687 (m), 603 (m), 528 (m). The presence of Ni^{2+} ions and iminodiacetic acid in the synthetic mixture is necessary to get crystals although they are not present in the final compound.

Preparation of $Na_7Mn^{II}_2Fe^{II}_4Fe^{III}_4[P_4Mo_6O_{26}(OH)_5]_4(PO_4){\cdot}52H_2O$ (**Fe-Mn**): A mixture of $Na_2MoO_4{\cdot}2H_2O$ (0.470 g, 1.95 mmol), metallic Mo (0.030 g, 0.31 mmol), 8 M H_3PO_4 (530 μL, 4.22 mmol), $(NH_4)_2Fe(SO_4)_2{\cdot}2H_2O$ (0.280 g, 0.70 mmol), $MnCl_2{\cdot}4H_2O$ (0.058 g, 0.29 mmol), iminodiacetic acid (0.100 g, 0.75 mmol) and H_2O (4 mL) was stirred and the pH was adjusted to 2.5 with 4 M HCl (pH_f = 2.6). Dark red hexagonal crystals were isolated after filtration and sonication in ethanol (0.270 g, 44.0 % based on Mo). Metal composition was checked by EDX analysis: P/Mo = 0.71 (calc.: 0.67); Mn/Fe = 0.25 (calc : 0.25); Fe/Mo = 0.33 (calc :0.48); Fe/Na 1.10 (1.14). IR (ν/cm^{-1}): 1624 (m), 1427 (m), 1190 (m), 1112 (sh), 1073 (s), 1043 (s), 1001 (s), 955 (s), 918 (s), 785 (m), 701 (m), 595 (m), 537 (m).

Crystal Structure Determination. Single crystal X-ray diffraction data collections were carried out by using a Bruker

AXS BV diffractometer equipped with a CCD bidimensional detector using the monochromatised wavelength λ(Mo Kα) = 0.71073 Å. Absorption corrections were based on multiple and symmetry-equivalent reflections in the data set using the SADABS program based on the method of Blessing. The structures were solved by direct methods and refined by full-matrix least-squares using the SHELX-TL package. In the structure of **Ru(bpy)-Co**, one of the Co ions is disordered over two positions (Co3A and Co3B, with space occupation factors equal to 0.7 and 0.3, respectively) as well as one of the P atoms (P4A and P4B, with space occupation factors equal to 0.5 and 0.5, respectively). A disorder on one of the phosphate group is also observed in the structure of **Ru(bpy)-Mn**. Crystallographic data are given in Table S1 and the complete data can be found in the cif file as Supporting Information. Selected bond distances and valence bond calculations are given in Figures S5-S7. Valence bond calculations confirm the oxidation state of the Mo, Mn, Co and Fe ions and indicate the presence of protons on bridging oxygen atoms of the POMs.

Powder X-ray diffraction data were obtained on a Brüker D5000 diffractometer using Cu radiation (1.54059 Å). EDX measurements were performed on a JEOL JSM 5800LV apparatus. Thermogravimetry analyses (TGA) were performed on a Mettler Toledo TGA/DSC 1, STARe System apparatus under oxygen flow (50 mL min^{-1}) at a heating rate of 5°C min^{-1} up to 700°C.

X-ray photoemission spectroscopy (XPS) measurements. XPS surface chemical analyses were carried out with a Thermo Fisher Scientific Nexsa spectrometer using a monochromatic Al Kα X-Ray source (1486.6 eV) and a dual flood gun (low energy electron and ion). A 400 µm X-ray spot was focused on a small amount of **Fe-Mn** compound and reference materials (powders) previously placed onto a carbon tape. The references used for Fe were $FeCl_2$ for Fe(II) and $NH_4Fe(SO_4)_2$ for Fer(III). Survey spectra were acquired using a Constant Analyser Energy (CAE) mode of 200 eV and an energy step size of 1 eV. Core levels spectra of interest were acquired using a CAE mode of 50 eV and an energy step size of 0.1 eV. Data were processed using Thermo Fisher Scientific Avantage© data system. Quantification was obtained from the photopeak areas after a Shirley type background subtraction and the use of "ALTHERMO1" library as sensitivity factor collection. All the binding energies were corrected to position the C-C contribution from the C1s spectrum at 284.8 eV. Spectrometer energy calibration is accomplished according to Thermo Fisher Scientific procedure using metallic Cu, Ag and Au internal references.

Photocatalytic experiments. If no contrary indication, all photocatalytic experiments where run in H_2O/TEOA 14:1 (v/v), with 30 mL of sample and 10 mg of catalyst finely ground in a mortar and 0.01 mmol of $[Ru(bpy)_3]Cl_2$. Photochemical reactions were performed using a 280 W, high-pressure Xe arc lamp (Newport Instruments). The beam was passed through a water infrared filter, a collimating lens, and a filter holder equipped with a 415 nm band-pass filter (Asahi Spectra). Samples were saturated with CO_2 via directly bubbling CO_2 through the solution mixture for 30 min. During irradiation, the samples were vigorously stirred and aliquots of gas were analyzed. H_2 measurements (aliquots of 50 µL of the headspace) were performed by gas chromatography on a Shimadzu GC-2014 equipped with a Quadrex column and a Thermal Conductivity Detector and using N_2 as a carrier gas. Formate was analyzed using a Metrohm 883 Basic IC plus ionic exchange chromatography instrument, using a Metrosep A Supp 5 column and a conductivity detector. A typical measurement requires the sampling of 200 µL of solution, followed by a 100 dilution in deionized 18 MΩ water and injection of 20 µL into the IC chromatograph. No H_2 nor formate was detected. CO and CH_4 were measured using a Shimadzu GC-2010 Plus gas chromatograph, fitted with a S9 Restek Shin Carbon column, helium carrier gas, a methanizer, and a flame ionization detector.

Computational Details. DFT calculations were carried out with the Gaussian09[51] software. The models of the reactive regions of the crystals were generated from X-ray crystal structures, from which $M\{P_4Mo_6\}\text{-}(M)_n\text{-}\{P_4Mo_6\}M$ patterns were extracted and protonated according to the results of the valence bond analysis. To reduce the complexity of the calculations, we replaced the terminal M ions and two of the four interstitial Co centers belonging to the same dimer by closed-shell Zn(II) ions. The terminal Zn centers were saturated with three aqua ligands, and their relative position was constrained during the geometry optimizations to account for the rigidity of the crystal lattice. Geometry optimizations and energy calculations were performed at the B3LYP level[52,53] and solvent effects of water were included by means of the IEF-PCM implicit solvent model[54] as implemented in Gaussian 09. All transition metal atoms were described by the Stuttgart relativistic small core pseudopotential and with the associated double-ζ valence basis set.[55] The Dunning-type correlation consistent double-ζ polarized basis set (cc-pVDZ)[56] was used for the remaining atoms. Calculations on smaller cluster models of Mn(II), Co(II) and Fe(II) sites of the materials were conducted at the same level of theory. In these models, the oxygen atoms of the phosphate groups directly coordinated to the POM were saturated with hydrogen atoms, and their positions were constrained during the geometry optimizations to maintain the configuration of the metal environment in the real system. The standard-state correction of +1.89 kcal·mol^{-1} to change from a reference state of 1 atm to the standard state of 1 M in solution at 25ºC was applied to the free-energies of all the species but water, for which the standard state corresponds to a higher concentration being the solvent in this reaction. For water molecule, according to a density of 0.997 g·cm^{-3}, the correction thus increases up to +4.3 kcal·mol^{-1}.[57] As the free energy of the $CO_2^{\bullet-}$ species in aqueous solution is not properly described by static DFT with implicit solvent models[58] we estimated this value from the free energy of the neutral CO_2 and the experimental redox potential of -2.15 V *vs* SCE for the $CO_2/CO_2^{\bullet-}$ pair (-1.90 V *vs* NHE).[45] Mn(II), Co(II) and Fe(II) ions were computed with M_s values of 5/2, 3/2 and 2, respectively; and the spin state for the Mn (the case that we analyzed in more detail) was found not change along the reaction coordinate. The Density of States (DOS) was obtained from the electronic structure analysis of the B3LYP-optimized geometries of the structural models represented in Figure 5a and S24a by means of the Multiwfn software[59] and using Gaussian-type broadening functions with a full width at half height of 0.3 eV.

The absorption spectra of cluster models of **Ru(bpy)-Mn** were simulated by means of time-dependent DFT[60,61] using the Gaussian 09 code. The long-range corrected ωB97X-D functional[62] was adopted for these calculations in conjunction with the LANL2DZ basis set[63] (and associated pseudopotentials) supplemented with an f-type polarization shell[64] for metal centers and a 6-31G(d,p) basis set[65–67] for the remaining elements. Additional tests with other methodologies were performed to address the influence of the nature of the basis functions and the density functional, all them providing the same qualitative description (see SI for further details).

AUTHOR INFORMATION

Corresponding Author

* E-mail: caroline.mellot-draznieks@college-de-france.fr, anne.dolbecq@uvsq.fr.

Author Contributions

The manuscript was written through contributions of all authors. ‡ Y. B. and A. S.-D. contributed equally.

ASSOCIATED CONTENT

Supporting Information. Comparison of the experimental X-ray powder patterns and of the powder patterns calculated from the structure solved from single crystal X-ray diffraction, crystallographic data, selected bond distances, bond valence sums, infrared spectra, TGA analysis, additional figures of the structure, additional computational data including simulated absorption spectra, spin density distributions, MO diagrams and Cartesian coordinates for optimized geometries. This material is available free of charge via the Internet at http://pubs.acs.org. Accession codes: Crystallographic data for new structures reported herein were deposited with the Cambridge Crystallographic Data Centre and allocated the deposition numbers CCDC 2111779 (**Ru(bpy)-Co**), 2111780 (**Ru(bpy)-Mn**) and 2111781 (**Fe-Mn**). These data can be obtained free of charge from the Cambridge Crystallographic Data Centre via www.ccdc.cam.ac.uk/data_request/cif.

Funding Sources

This work was supported by CNRS, UVSQ, the Ministère de l'Enseignement Supérieur, de la Recherche et de l'Innovation, the French National Research Agency (ANR) as part of the "Investissements d'Avenir" program n°ANR-11-IDEX-0003-02 and CHARMMMAT ANR-11-LABX-0039. The calculations have been performed using the HPC national resources from GENCI (CINES/TGCC) through Grant 2016-097343.

REFERENCES

(1) Wang, S.-S.; Yang, G.-Y. Recent Advances in Polyoxometalate-Catalyzed Reactions. *Chem. Rev.* **2015**, *115* (11), 4893–4962.

(2) Weinstock, I. A.; Schreiber, R. E.; Neumann, R. Dioxygen in Polyoxometalate Mediated Reactions. *Chem. Rev.* **2018**, *118* (5), 2680–2717.

(3) Samaniyan, M.; Mirzaei, M.; Khajavian, R.; Eshtiagh-Hosseini, H.; Streb, C. Heterogeneous Catalysis by Polyoxometalates in Metal–Organic Frameworks. *ACS Catal.* **2019**, *9* (11), 10174–10191.

(4) Buru, C. T.; Farha, O. K. Strategies for Incorporating Catalytically Active Polyoxometalates in Metal–Organic Frameworks for Organic Transformations. *ACS Appl. Mater. Interfaces* **2020**, *12* (5), 5345–5360.

(5) Lefebvre, F. Synthesis, Characterization and Applications in Catalysis of Polyoxometalate/Zeolite Composites. *Inorganics* **2016**, *4* (2), 13.

(6) Mialane, P.; Mellot-Draznieks, C.; Gairola, P.; Duguet, M.; Benseghir, Y.; Oms, O.; Dolbecq, A. Heterogenisation of Polyoxometalates and Other Metal-Based Complexes in Metal–Organic Frameworks: From Synthesis to Characterisation and Applications in Catalysis. *Chem. Soc. Rev.* **2021**, *50* (10), 6152–6220.

(7) Lauinger, S. M.; Yin, Q.; Geletii, Y. V.; Hill, C. L. Polyoxometalate Multielectron Catalysts in Solar Fuel Production. In *Advances in Inorganic Chemistry*; Elsevier, 2017; Vol. 69, pp 117–154.

(8) Lin, J.; Han, Q.; Ding, Y. Catalysts Based on Earth-Abundant Metals for Visible Light-Driven Water Oxidation Reaction. *Chem. Rec.* **2018**, *18* (11), 1531–1547.

(9) Han, Q.; Ding, Y. Recent Advances in the Field of Light-Driven Water Oxidation Catalyzed by Transition-Metal Substituted Polyoxometalates. *Dalton Trans.* **2018**, *47* (25), 8180–8188.

(10) Soriano-López, J.; Musaev, D. G.; Hill, C. L.; Galán-Mascarós, J. R.; Carbó, J. J.; Poblet, J. M. Tetracobalt-Polyoxometalate Catalysts for Water Oxidation: Key Mechanistic Details. *J. Catal.* **2017**, *350*, 56–63.

(11) Cao, Y.; Chen, Q.; Shen, C.; He, L. Polyoxometalate-Based Catalysts for CO2 Conversion. **2019**, 26.

(12) Li, N.; Liu, J.; Dong, B.-X.; Lan, Y.-Q. Polyoxometalate-Based Compounds for Photo- and Electrocatalytic Applications. *Angew. Chem. Int. Ed.* **2020**, *59* (47), 20779–20793.

(13) Khenkin, A. M.; Efremenko, I.; Weiner, L.; Martin, J. M. L.; Neumann, R. Photochemical Reduction of Carbon Dioxide Catalyzed by a Ruthenium-Substituted Polyoxometalate. *Chem. – Eur. J.* **2010**, *16* (4), 1356–1364.

(14) Girardi, M.; Blanchard, S.; Griveau, S.; Simon, P.; Fontecave, M.; Bedioui, F.; Proust, A. Electro-Assisted Reduction of CO_2 to CO and Formaldehyde by $(TOA)_6[\alpha\text{-}SiW_{11}O_{39}Co(\_)]$ Polyoxometalate. *Eur. J. Inorg. Chem.* **2015**, *2015* (22), 3642–3648.

(15) Girardi, M.; Platzer, D.; Griveau, S.; Bedioui, F.; Alves, S.; Proust, A.; Blanchard, S. Assessing the Electrocatalytic Properties of the Cp^*Rh^{III} $^{2+}$-Polyoxometalate Derivative $[H_2PW_{11}O_{39}Rh^{III}Cp^*(OH_2)]^{3-}$ towards CO_2 Reduction. *Eur. J. Inorg. Chem.* **2019**, *2019* (3–4), 387–393.

(16) Du, J. Polyoxometalate-Based Electron Transfer Modulation for Efficient Electrocatalytic Carbon Dioxide Reduction. *Chem. Sci.* **2020**, 9.

(17) Barman, S.; Sreejith, S. S.; Garai, S.; Pochamoni, R.; Roy, S. Selective Photocatalytic Carbon Dioxide Reduction by a Reduced Molybdenum-Based Polyoxometalate Catalyst. *ChemPhotoChem* **2019**, *3* (2), 93–100.

(18) Li, X.-X.; Liu, J.; Zhang, L.; Dong, L.-Z.; Xin, Z.-F.; Li, S.-L.; Huang-Fu, X.-Q.; Huang, K.; Lan, Y.-Q. Hydrophobic Polyoxometalate-Based Metal-Organic Framework for Efficient CO_2 Photoconversion. *ACS Appl Mater Interfaces* **2019**, 6.

(19) Xie, S.-L.; Liu, J.; Dong, L.-Z.; Li, S.-L.; Lan, Y.-Q.; Su, Z.-M. Hetero-Metallic Active Sites Coupled with Strongly Reductive Polyoxometalate for Selective Photocatalytic CO_2-to-CH_4 Conversion in Water. *Chem. Sci.* **2019**, *10* (1), 185–190.

(20) Xu, H.; You, S.; Lang, Z.; Sun, Y.; Sun, C.; Zhou, J.; Wang, X.; Kang, Z.; Su, Z. Highly Efficient Photoreduction of

Low-Concentration CO_2 to Syngas by Using a Polyoxometalates/Ru^{II} Composite. *Chem. – Eur. J.* **2020**, *26* (12), 2735–2740.

(21) Du, J.; Ma, Y.; Xin, X.; Na, H.; Zhao, Y.; Tan, H.; Han, Z.; Li, Y.; Kang, Z. Reduced Polyoxometalates and Bipyridine Ruthenium Complex Forming a Tunable Photocatalytic System for High Efficient CO_2 Reduction. *Chem. Eng. J.* **2020**, *398*, 125518.

(22) Du, Z.-Y.; Chen, Z.; Kang, R.-K.; Han, Y.-M.; Ding, J.; Cao, J.-P.; Jiang, W.; Fang, M.; Mei, H.; Xu, Y. Two 2D Layered P_4Mo_6 Clusters with Potential Bifunctional Properties: Proton Conduction and CO_2 Photoreduction. *Inorg. Chem.* **2020**.

(23) du Peloux, C.; Mialane, P.; Dolbecq, A.; Marrot, J.; Varret, F.; Sécheresse, F. Three-Dimensional Mn/Fe Molybdenum(V) Phosphates. *Solid State Sci.* **2004**, *6* (7), 719–724.

(24) du Peloux, C.; Dolbecq, A.; Mialane, P.; Marrot, J.; Rivière, E.; Sécheresse, F. A New Two-Dimensional Molybdenum(V) Nickel Phosphate Built Up of $[H_{18}(Mo_{16}O_{32})Ni_{16}(PO_4)_{26}(OH)_6(H_2O)_8]^{18-}$ Wheels. *Inorg. Chem.* **2002**, *41* (26), 7100–7104.

(25) du Peloux, C.; Dolbecq, A.; Mialane, P.; Marrot, J.; Riviere, E.; Secheresse, F. A New Family of Layered Molybdenum(v) Cobalto-Phosphates Built up of $[H_{14}(Mo_{16}O_{32})Co_{16}(PO_4)_{24}(H_2O)_{20}]^{10-}$ Wheels. *Angew. Chem.-Int. Ed.* **2001**, *40* (13), 2455-+.

(26) du Peloux, C.; Mialane, P.; Dolbecq, A.; Marrot, J.; Riviere, E.; Secheresse, F. Synthesis, Crystal Structure and Magnetic Properties of New Molybdenum(V) Phosphates Containing Mn^{2+} or Co^{2+} with Three-Dimensional Structures Directed by the Nature of the Transition Metal. *J. Mater. Chem.* **2001**, *11* (12), 3392–3396.

(27) Salomon, W.; Paille, G.; Gomez-Mingot, M.; Mialane, P.; Marrot, J.; Roch-Marchal, C.; Nocton, G.; Mellot-Draznieks, C.; Fontecave, M.; Dolbecq, A. Effect of Cations on the Structure and Electrocatalytic Response of Polyoxometalate-Based Coordination Polymers. *Cryst. Growth Des.* **2017**, *17* (4), 1600–1609.

(28) Soriano-López, J.; Song, F.; Patzke, G. R.; Galan-Mascaros, J. R. Photoinduced Oxygen Evolution Catalysis Promoted by Polyoxometalate Salts of Cationic Photosensitizers. *Front. Chem.* **2018**, *6*, 302.

(29) Hawecker, J.; Lehn, J.-M.; Ziessel, R. Photochemical Reduction of Carbon Dioxide to Formate Mediated by Ruthenium Bipyridine Complexes as Homogeneous Catalysts. *J. Chem. Soc. Chem. Commun.* **1985**, No. 2, 56–58.

(30) Stanbury, M.; Compain, J.-D.; Chardon-Noblat, S. Electro and Photoreduction of CO_2 Driven by Manganese-Carbonyl Molecular Catalysts. *Coord. Chem. Rev.* **2018**, *361*, 120–137.

(31) Davethu, P. A.; de Visser, S. P. CO_2 Reduction on an Iron-Porphyrin Center: A Computational Study. *J. Phys. Chem. A* **2019**, *123* (30), 6527–6535.

(32) Shakeri, J.; Farrokhpour, H.; Hadadzadeh, H.; Joshaghani, M. Photoreduction of CO_2 to CO by a Mononuclear Re(I) Complex and DFT Evaluation of the Photocatalytic Mechanism. *RSC Adv.* **2015**, *5* (51), 41125–41134.

(33) Wang, F.; Cao, B.; To, W.-P.; Tse, C.-W.; Li, K.; Chang, X.-Y.; Zang, C.; Chan, S. L.-F.; Che, C.-M. The Effects of Chelating N4 Ligand Coordination on Co(II)-Catalysed Photochemical Conversion of CO_2 to CO: Reaction Mechanism and DFT Calculations. *Catal. Sci. Technol.* **2016**, *6* (20), 7408–7420.

(34) Wang, F.; Neumann, R.; de Graaf, C.; Poblet, J. M. Photoreduction Mechanism of CO_2 to CO Catalyzed by a Three-Component Hybrid Construct with a Bimetallic Rhenium Catalyst. *ACS Catal.* **2021**, 1495–1504.

(35) Yan, Z.-H.; Ma, B.; Li, S.-R.; Liu, J.; Chen, R.; Du, M.-H.; Jin, S.; Zhuang, G.-L.; Long, L.-S.; Kong, X.-J.; Zheng, L.-S. Encapsulating a Ni(II) Molecular Catalyst in Photoactive Metal–Organic Framework for Highly Efficient Photoreduction of CO_2. *Sci. Bull.* **2019**, *64* (14), 976–985.

(36) Zhu, C.-Y.; Zhang, Y.-Q.; Liao, R.-Z.; Xia, W.; Hu, J.-C.; Wu, J.; Liu, H.; Wang, F. Photocatalytic Reduction of CO_2 to CO and Formate by a Novel Co(II) Catalyst Containing a Cis-Oxygen Atom: Photocatalysis and DFT Calculations. *Dalton Trans.* **2018**, *47* (37), 13142–13150.

(37) Shen, J.; Kolb, M. J.; Göttle, A. J.; Koper, M. T. M. DFT Study on the Mechanism of the Electrochemical Reduction of CO_2 Catalyzed by Cobalt Porphyrins. *J. Phys. Chem. C* **2016**, *120* (29), 15714–15721.

(38) Isegawa, M.; Sharma, A. K. CO_2 Reduction by a Mn Electrocatalyst in the Presence of a Lewis Acid: A DFT Study on the Reaction Mechanism. *Sustain. Energy Fuels* **2019**, *3* (7), 1730–1738.

(39) López, X.; Carbó, J. J.; Bo, C.; Poblet, J. M. Structure, Properties and Reactivity of Polyoxometalates: A Theoretical Perspective. *Chem. Soc. Rev.* **2012**, *41* (22), 7537–7571.

(40) Durham, B.; Caspar, J. V.; Nagle, J. K.; Meyer, T. J. Photochemistry of Tris(2,2'-Bipyridine)Ruthenium(2+) Ion. *J. Am. Chem. Soc.* **1982**, *104* (18), 4803–4810.

(41) Cohen, S. G.; Parola, A.; Parsons, G. H. Photoreduction by Amines. *Chem. Rev.* **1973**, *73* (2), 141–161.

(42) Cohen, S. G.; Baumgarten, R. J. Photoreduction of Benzophenone by Amines. Photochemical Oxidative Deamination1. *J. Am. Chem. Soc.* **1965**, *87* (13), 2996–2997.

(43) Pellegrin, Y.; Odobel, F. Sacrificial Electron Donor Reagents for Solar Fuel Production. *Comptes Rendus Chim.* **2017**, *20* (3), 283–295.

(44) Kirch, M.; Lehn, J.-M.; Sauvage, J.-P. Hydrogen Generation by Visible Light Irradiation of Aqueous Solutions of Metal Complexes. An Approach to the Photochemical Conversion and Storage of Solar Energy. *Helv. Chim. Acta* **1979**, *62* (4), 1345–1384.

(45) Morris, A. J.; Meyer, G. J.; Fujita, E. Molecular Approaches to the Photocatalytic Reduction of Carbon Dioxide for Solar Fuels. *Acc. Chem. Res.* **2009**, *42* (12), 1983–1994.

(46) Janik, I.; Tripathi, G. N. R. The Nature of the CO_2^- Radical Anion in Water. *J. Chem. Phys.* **2016**, *144* (15), 154307.

(47) Liu, P.; Zhao, J.; Liu, J.; Zhang, M.; Bu, Y. Ab Initio Molecular Dynamics Simulations Reveal Localization and Time Evolution Dynamics of an Excess Electron in Heterogeneous CO_2–H_2O Systems. *J. Chem. Phys.* **2014**, *140* (4), 044318.

(48) Goez, M.; von Ramin-Marro, D.; Othman Musa, M. H.; Schiewek, M. Photoionization of $[Ru(Bpy)_3]^{2+}$: A Catalytic Cycle with Water as Sacrificial Donor. *J. Phys. Chem. A* **2004**, *108* (6), 1090–1100.

(49) Alnaed, M. K.; Endicott, J. F. Chemical Scavenging Yields for Short-Lived Products from the Visible Light Photoionization of the Tris(Bipyridine)Ruthenium(II) Triplet Metal-to-Ligand Charge-Transfer Excited State. *J. Phys. Chem. A* **2018**, *122* (48), 9251–9266.

(50) Broomhead, J. A.; Young, C. G.; Hood, P. Tris(2,2″-Bipyridine)Ruthenium(II) Dichloride Hexahydrate. In *Inorganic Syntheses*; John Wiley & Sons, Ltd, 1990; pp 338–340.

(51) Gaussian 09, Revision D.01, Frisch, M. J.; Trucks, G. W.; Schlegel, H. B.; Scuseria, G. E.; Robb, M. A.; Cheeseman, J. R.; Scalmani, G.; Barone, V.; Mennucci, B.; Petersson, G. A.; Nakatsuji, H.; Caricato, M.; Li, X.; Hratchian, H. P.; Izmaylov, A. F.; Bloino, J.; Zheng, G.; Sonnenberg, J. L.; Hada, M.; Ehara, M.; Toyota, K.; Fukuda, R.; Hasegawa, J.; Ishida, M.; Nakajima, T.; Honda, Y.; Kitao, O.; Nakai, H.; Vreven, T.; Montgomery, J. A., Jr.; Peralta, J. E.; Ogliaro, F.; Bearpark, M.; Heyd, J. J.; Brothers, E.; Kudin, K. N.; Staroverov, V. N.; Kobayashi, R.; Normand, J.; Raghavachari, K.; Rendell, A.; Burant, J. C.; Iyengar, S. S.; Tomasi, J.; Cossi, M.; Rega, N.; Millam, J. M.; Klene, M.; Knox, J. E.; Cross, J. B.; Bakken, V.; Adamo, C.; Jaramillo, J.; Gomperts, R.; Stratmann, R. E.; Yazyev, O.; Austin, A. J.; Cammi, R.; Pomelli, C.; Ochterski, J. W.; Martin, R. L.; Morokuma, K.; Zakrzewski, V. G.; Voth, G. A.; Salvador, P.; Dannenberg, J. J.; Dapprich, S.; Daniels, A. D.; Farkas, Ö.; Foresman, J. B.; Ortiz, J. V.; Cioslowski, J.; Fox, D. J. Gaussian, Inc., Wallingford CT, 2009.

(52) Becke, A. D. Density-functional Thermochemistry. III. The Role of Exact Exchange. *J. Chem. Phys.* **1993**, *98* (7), 5648–5652.

(53) Stephens, P. J.; Devlin, F. J.; Chabalowski, C. F.; Frisch, M. J. Ab Initio Calculation of Vibrational Absorption and Circular Dichroism Spectra Using Density Functional Force Fields. *J. Phys. Chem.* **1994**, *98* (45), 11623–11627.

(54) Cancès, E.; Mennucci, B.; Tomasi, J. A New Integral Equation Formalism for the Polarizable Continuum Model: Theoretical Background and Applications to Isotropic and Anisotropic Dielectrics. *J. Chem. Phys.* **1997**, *107* (8), 3032–3041.

(55) Andrae, D.; Häußermann, U.; Dolg, M.; Stoll, H.; Preuß, H. Energy-Adjustedab Initio Pseudopotentials for the Second and Third Row Transition Elements. *Theor. Chim. Acta* **1990**, *77* (2), 123–141.

(56) Schaefer, H. F. *Methods of Electronic Structure Theory*; Modern Theoretical Chemistry; Springer US, 1977.

(57) Mihaylov, T. T.; Ly, H. G. T.; Pierloot, K.; Parac-Vogt, T. N. Molecular Insight from DFT Computations and Kinetic Measurements into the Steric Factors Influencing Peptide Bond Hydrolysis Catalyzed by a Dimeric Zr(IV)-Substituted Keggin Type Polyoxometalate. *Inorg. Chem.* **2016**, *55* (18), 9316–9328.

(58) McNeill, A. S.; Dixon, D. A. Energetics of CO2– in Aqueous Solution. *J. Phys. Chem. A* **2019**, *123* (6), 1243–1259.

(59) Lu, T.; Chen, F. Multiwfn: A multifunctional wavefunction analyzer *J. Comput. Chem.* **2012**, *33*, 580-592.

(60) Bauernschmitt, R.; Ahlrichs, R. Treatment of Electronic Excitations within the Adiabatic Approximation of Time Dependent Density Functional Theory. *Chem. Phys. Lett.* **1996**, *256* (4), 454–464.

(61) Marques, M. a. l.; Gross, E. k. u. Time-Dependent Density Functional Theory. *Annu. Rev. Phys. Chem.* **2004**, *55* (1), 427–455.

(62) Chai, J.-D.; Head-Gordon, M. Long-Range Corrected Hybrid Density Functionals with Damped Atom–Atom Dispersion Corrections. *Phys. Chem. Chem. Phys.* **2008**, *10* (44), 6615–6620.

(63) Hay, P. J.; Wadt, W. R. Ab Initio Effective Core Potentials for Molecular Calculations. Potentials for the Transition Metal Atoms Sc to Hg. *J. Chem. Phys.* **1985**, *82* (1), 270–283.

(64) Ehlers, A. W.; Böhme, M.; Dapprich, S.; Gobbi, A.; Höllwarth, A.; Jonas, V.; Köhler, K. F.; Stegmann, R.; Veldkamp, A.; Frenking, G. A Set of F-Polarization Functions for Pseudo-Potential Basis Sets of the Transition Metals Sc-Cu, Y-Ag and La-Au. *Chem. Phys. Lett.* **1993**, *208* (1), 111–114.

(65) Francl, M. M.; Pietro, W. J.; Hehre, W. J.; Binkley, J. S.; Gordon, M. S.; DeFrees, D. J.; Pople, J. A. Self-consistent Molecular Orbital Methods. XXIII. A Polarization-type Basis Set for Second-row Elements. *J. Chem. Phys.* **1982**, *77* (7), 3654–3665.

(66) Hariharan, P. C.; Pople, J. A. The Influence of Polarization Functions on Molecular Orbital Hydrogenation Energies. *Theor. Chim. Acta* **1973**, *28* (3), 213–222.

(67) Hehre, W. J.; Ditchfield, R.; Pople, J. A. Self—Consistent Molecular Orbital Methods. XII. Further Extensions of Gaussian—Type Basis Sets for Use in Molecular Orbital Studies of Organic Molecules. *J. Chem. Phys.* **1972**, *56* (5), 2257–2261.

SYNOPSIS TOC